NJC

PAPER

Cite this: *New J. Chem.*, 2021, **45**, 2090

Lanthanide metal–organic frameworks for catalytic oxidation of olefins†

Y. B. N. Tran[ab] and Phuong T. K. Nguyen *[ab]

Received 21st November 2020,
Accepted 6th January 2021

DOI: 10.1039/d0nj05685e

rsc.li/njc

Two isostructural lanthanide metal–organic frameworks (Ln-MOF-589, Ln = La^{3+}, Ce^{3+}), constructed from a tetratopic linker, benzoimidephenanthroline tetracarboxylic acid (H_4BIPA-TC), have been solvothermally synthesized and characterized. These Ln-MOF-589 materials consist of Lewis acid $[Ln_2(\text{-COO})_6(\text{-COOH})_2(H_2O)_6]$ units and a naphthalene diimide core, which exhibited promising catalytic activity for the oxidation of olefins. Among them, Ce-MOF-589 exhibited outstanding performance with high conversions of styrene and cyclohexene (94 and 90%, respectively), and good selectivities towards styrene oxide and 2-cyclohexen-1-one (85, and 95%, respectively). Notably, the catalytic activity of Ce-MOF-589 outperformed that of homogeneous and heterogeneous catalysts, and representative MOFs. Also, Ce-MOF-589 can be recycled for at least up to six cycles with no significant loss of catalytic performance.

Introduction

Catalytic oxidation of alkenes/olefins to fine chemicals represents a significant process in organic synthesis and industrial production. The selective oxidation of olefins into epoxides has attracted tremendous attention since the epoxide products have a wide range of applications, including precursors for pharmaceutical synthesis and industrial intermediates for making valuable products such as epoxy resins, paints, and surfactants.[1] Allylic C–H oxidation of alkenes to the corresponding α,β-unsaturated enones or 1,4-enediones is particularly important in the synthesis of natural products and synthetic drug precursors.[2] Numerous studies have been devoted to the development of homogeneous and heterogeneous catalysts for the oxidation of olefins.[3] However, it remains a challenge to achieve high selectivity in oxidation reactions.[1–3] While many soluble metal complexes have been demonstrated to be active in oxidation reactions, several limitations remain, *e.g.*, corrosion, deposition on reactor walls, and difficulty in recovery and separation of the catalyst from the reaction media. These disadvantages can be overcome when using insoluble support-based catalysts embedded with homogeneous active species and heterogeneous catalysts.[4]

Metal–organic frameworks (MOFs) have emerged as a potential heterogeneous catalyst.[5–9] MOFs are one of the most widely studied crystalline materials constructed by combining inorganic metal clusters and organic linkers *via* strong bonds.[10] The variable functionalities, considerable thermal and chemical stability, and well-ordered distribution of multiple active sites inside MOFs' pores make them suitable candidates for heterogeneous catalysis for a variety of organic transformation reactions.[11–16] In particular, MOFs containing lanthanide (Ln) components and heteroatom-based functionalities have been demonstrated to be potential heterogeneous catalysts in the oxidation of olefins.[5,9,17–21] In particular, MOFs containing lanthanide (Ln) components and heteroatom-based functionalities have been demonstrated to be potential heterogeneous catalysts in the oxidation of olefins. In this respect, the Ce-UiO-66-$(CH_3)_2$ MOF was employed as the catalyst in the oxidation of styrene with the use of the TBHP oxidant, showing high conversion (91%) and low selectivities of benzaldehyde (40%) and styrene oxide (33%).[22] Another Cu-based MOF, $[Cu_2(bipy)_2(btec)]_\infty$, containing a bipyridine linker, was found to be a promising catalyst in the oxidation of olefins. The Cu-MOF showed an average conversion of styrene (61%) and low selectivity of styrene oxide (32%), while only 34% conversion of cyclohexene and 72% selectivity of 2-cyclohexen-1-one formation were achieved.[23]

Lanthanide-based MOFs (Ln-MOFs) constructed from lanthanide ions are emerging as attractive Lewis acid catalysts in various organic transformations.[24,25] Some Ln-based metals such as La and Ce, which are abundant and inexpensive rare earth elements, have been widely studied in many applications.[26–28] Ln ions have high oxidation states, which could induce the thermal robustness property of Ln-based frameworks. The large

---

[a] *Future Materials & Devices Laboratory, Institute of Fundamental and Applied Sciences, Duy Tan University, Ho Chi Minh City 700000, Vietnam. E-mail: nguyentkieuphuong1@duytan.edu.vn*

[b] *Faculty of Natural Sciences, Duy Tan University, Da Nang, 550000, Vietnam. E-mail: nguyentkieuphuong1@duytan.edu.vn*

† Electronic supplementary information (ESI) available: Experimental details, MOF preparation, PXRD, IR, TGA, NMR, SEM, N_2, CO_2 sorption, and catalytic study. See DOI: 10.1039/d0nj05685e

and variable coordination numbers of Ln ions prompt the formation of a high density of coordinated solvents binding to Ln sites, which, when removed, can produce unsaturated metal sites serving as Lewis acid sites.[29] However, the variable coordination of Ln-based metals assists in the construction of interpenetrating frameworks that have limited pore sizes and low surface areas. Otherwise, the variety of Ln sources could provide different strengths of Lewis acidity, resulting in diverse catalytic activities for acid-catalyzed reactions. Furthermore, Ln-MOFs containing Brønsted acid sites such as uncoordinated carboxylic groups (from organic linkers) and hydroxyl moieties (from water molecules coordinating to metal clusters) have been demonstrated to enhance the conversion and selectivity of various catalytic transformations.[30] Compared with the well-established studies on homogeneous lanthanide-based compounds and transition metal-based MOF catalysts, less has been reported on the development of heterogeneous Ln-MOFs for the catalytic oxidation of olefins.[21–23,31–33]

Recently, some MOFs with embedded *N*-hydroxyphthalimide (NHPI) revealed high selectivity in many oxidation transformations. In that context, NHPI species act as an organocatalyst, which together with a transition metal can act as the initiator of radical chain oxidation.[34,35] We previously reported the synthesis of a series of Ln-MOFs (MOF-589 to -592) constructed from a benzoimidephenanthroline tetracarboxylic acid (H_4BIPA-TC) linker and Ln^{3+} ions (Ln = Ce, Nd, Tb, Eu) and their wide applications in gas separation and catalytic transformations.[30,36] Notably, the naphthalene diimide core of the H_4BIPA-TC linker has high electron affinity, good charge carrier mobility, and excellent thermal and oxidative stability, making it a promising candidate for the catalytic oxidation process.[37]

Herein, we further employ the H_4BIPA-TC linker for synthesizing two isostructural Ln-based frameworks, called Ln-MOF-589 (Ln = La, Ce) (Fig. 1),[36] and examine their catalytic properties in the oxidation of olefins using anhydrous TBHP as an oxidant. The two Ln-MOF-589 materials showed efficient catalytic performance in the oxidation of styrene and cyclohexene under mild conditions (0.7 mol% of MOF catalyst, 75 °C, 10 h, solvent-free, and an N_2 environment). Among them, Ce-MOF-589 showed exceptional conversion of styrene and cyclohexene (94 and 90%, respectively) and high selectivities in the formation of styrene oxide (85%) and 2-cyclohexen-1-one (95%). Furthermore, Ce-MOF-589 was shown to be a robust catalyst and exhibited a heterogeneous nature with no significant loss of catalytic performance over five consecutive cycles.

Experimental section

Materials and analytical techniques

Full synthetic and characterization details are provided in the ESI† (Section S1). The H_4BIPA-TC linker was synthesized according to a literature procedure.[30] All chemicals for MOF synthesis and the catalytic reactions were purchased and used without purification. For comparison studies, commercial MOFs [HKUST-1 (Basolite C300), MOF-177 (Basolite Z377), ZIF-8 (Basolite Z1200), and Al-MIL-53 (Basolite A100)] were purchased and re-activated to obtain guest-free materials prior to conducting any experiment. Ce-MOF-76 was prepared according to a reported procedure (ESI,† Section S1).

Elemental microanalyses (EA) were performed using a LECO CHNS-932 analyzer. Fourier transform infrared (FT-IR) spectra were obtained on a Bruker Vertex 70 with samples being well-dispersed in KBr pellets and the output signals are depicted as vs, very strong; s, strong; m, medium; sh, shoulder; w, weak; vw, very weak; or br, broad. Thermal gravimetric analysis (TGA) curves were measured on a TA Q500 thermal analysis system with the sample held in a platinum pan under a continuous flow of air. Low-pressure N_2 and CO_2 adsorption isotherms were collected on a Micromeritics 3Flex with the use of He to estimate the dead space. A liquid N_2 bath was used for measurements at 77 K, and a circulating bath of ethylene glycol/water (1/1, v/v) was applied for measurements at 273, 283, and 298 K. Inductively coupled plasma mass spectroscopy (ICP-MS) data were collected on an Agilent ICP-MS 7700x instrument.

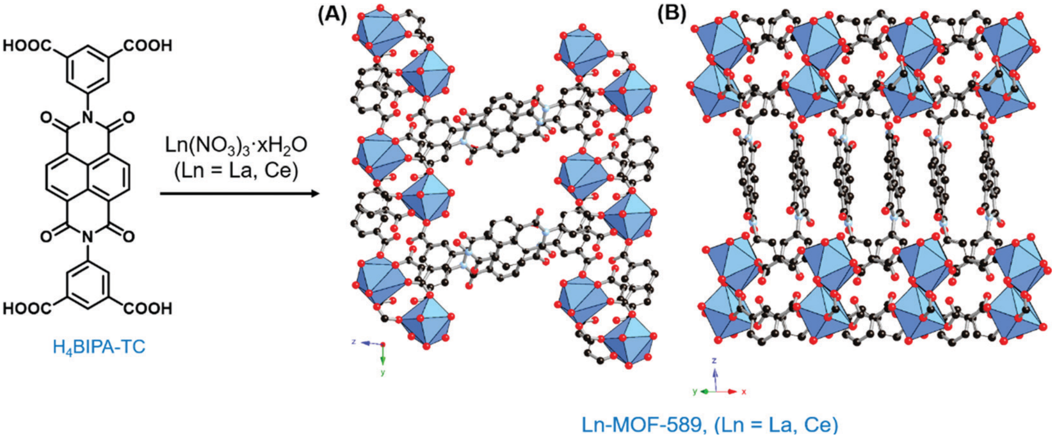

Fig. 1 Crystal structure of Ln-MOF-589. Linking of BIPA-TC^{4-} and $[Ln_2(\text{-COO})_6(\text{-COOH})_2(H_2O)_6]$ resulting in Ln-MOF-589. Color code: Ln, blue polyhedra; C, black; N, light blue; O, red. All H atoms of the benzene units are omitted for clarity. Redrawn from CCDC deposition 1843313.

To identify the products of the catalytic reaction, gas chromatography (GC) analysis was performed on an Agilent GC system 19091s-433 equipped with a mass selective detector (Agilent 5973N) (GC-MS) using a capillary HP-5MS 5% phenyl methyl silox column (30 m × 250 μm × 0.25 μm). The conversion, selectivity, and yield of the catalytic reactions were determined by GC analysis using an Agilent GC system 123-0132 equipped with a flame ionization detector (FID) and a capillary DB-1 ms column (30 m × 320 μm × 0.25 μm) with the use of chlorobenzene as an internal standard.

X-ray photoelectron spectroscopy (XPS) measurements were performed at Sungkyunkwan University (South Korea), using a Thermo Scientific K-Alpha X-ray photoelectron spectrometer with a non-monochromatic Al-Kα ($h\nu$ = 1486.6 eV) source. The binding energy data were calibrated with reference to the C 1s signal at 284.8 eV and O 1s signal at 531.0 eV. All the spectra were obtained with a pass energy of 25 eV, step increment of 0.1 eV, and total scans of 20. The experimental data were curve fitted with a Gaussian–Lorentzian model using Shirley background subtraction implemented in the Origin 9.0 program. The spin–orbit splitting and doublet intensities were fixed during the curve fitting.

X-ray diffraction analysis

Powder XRD (PXRD) patterns were measured using a Bruker D8 Advance diffractometer with Ni-filtered Cu Kα (λ = 1.54178 Å) radiation operated at 40 kV and 40 mA (1600 W). The system was outfitted with an anti-scattering shield to avoid incident diffuse radiation hitting the detector. MOF samples were mounted on zero background holders and then well-flattened using a spatula. PXRD patterns were recorded with a 2θ range from 3 to 50°, a step size of 0.02°, and a fixed count time of 1 s per step.

Synthesis of Ln-MOF-589

Ce-MOF-589. Ce-MOF-589 was prepared according to a published procedure.[36] EA of activated sample: calcd for $CeC_{30}H_{13}N_2O_{13}$ = [Ce(HBIPA-TC)]·H_2O: C, 48.70; H, 1.75; N, 3.74. Found: C, 48.51; H, 1.89; N, 3.68. FT-IR (KBr, 4000–400 cm^{-1}): 3425 (s, br), 1714 (s), 1678 (s), 1618 (s), 1578 (s), 1552 (s), 1447 (s), 1388 (s), 1350 (s), 1255 (s), 1199 (w), 1120 (w), 985 (vw), 952 (vw), 912 (vw), 883 (vw), 779 (w), 767 (w), 745 (w), 721 (vw), 677 (w), 652 (vw), 609 (vw).

La-MOF-589. $La(NO_3)_3 \cdot xH_2O$ (0.044 g, 0.01 mmol) and H_4BIPA-TC (0.060 g, 0.01 mmol) were inserted in a glass 8 mL vial containing a mixture of H_2O (2 mL), DMA (1 mL), and CH_3COOH (400 μL). The vial was accordingly sealed and heated to 120 °C for 15 h in an isothermal oven, yielding yellow block crystals of La-MOF-589. The as-synthesized La-MOF-589 was washed with DMF (3 × 10 mL) once a day for 3 days and accordingly exchanged in anhydrous EtOH (3 × 10 mL) once a day for 3 days. The solid was then dried at ambient temperature under a vacuum for 18 h, followed by heating at 60 °C for an additional 24 h to yield an activated sample. EA of activated sample: calcd for $LaC_{30}H_{13}N_2O_{13}$ = [La(HBIPA-TC)]·H_2O: C, 48.15; H, 1.75; N, 3.74. Found: C, 48.26; H, 1.66; N, 3.56. FT-IR (KBr, 4000–400 cm^{-1}): 3425 (s, br), 1714 (s), 1678 (s), 1618 (s), 1578 (s), 1552 (s), 1447 (s), 1388 (s), 1350 (s), 1255 (s), 1199 (w), 1120 (w), 985 (vw), 952 (vw), 912 (vw), 883 (vw), 779 (w), 767 (w), 745 (w), 721 (vw), 677 (w), 652 (vw), 609 (vw).

Catalytic studies

For the catalytic oxidation, the reaction was performed in a 25 mL two-necked Schlenk-flask which is connected to a condenser. The flask was then placed in a temperature-controlled oil bath and the reaction was carried out under a nitrogen atmosphere. In a typical reaction, the flask was charged with the catalyst (0.7 mol%, calculated based on metal sites), styrene or cyclohexene (5 mmol), and anhydrous *tert*-butyl hydroperoxide (TBHP in decane, 10 mmol). The reaction mixture was evacuated thoroughly to remove gas impurities and purged three times with N_2. The reaction mixture was stirred at 75 °C for 10 h. The progress of the reaction was monitored by analyzing regularly taken aliquots with GC. After completion of the reaction, the MOF catalyst was isolated by centrifugation, and an aliquot of the reaction was analyzed by GC-FID using chlorobenzene as the internal standard. For the recycling experiment, the recovered catalyst was rinsed with ethanol (3 × 3 mL) before heating at 60 °C under a vacuum for 24 h and then reused for the next cycles. To emphasize the reproducibility of the catalytic results, all catalytic reactions were conducted three times, and the results were obtained with standard deviations.

Results and discussion

Synthesis and structural characterization

The organic H_4BIPA-TC linker was synthesized by a one-step condensation reaction of 1,4,5,8-naphthalenetetracarboxlic dianhydride and 5-aminoisophthalic acid. The preparation of La-MOF-589 was accomplished in direct analogy with Ce-MOF-589,[30,36] in which two yellow-block Ln-MOF-589 (Ln = La, Ce) crystals were obtained by solvothermal reactions between H_4BIPA-TC and hydrated $Ln(NO_3)_3$ (Ln = La, Ce) in a solvent mixture of water, DMA, and CH_3COOH. The resulting microcrystalline Ln-MOF-589 (Ln = La, Ce) materials were achieved in high yield (>60%) and exhibited a homogeneous morphology when examined using optical microscope images (Fig. S1 and S2, ESI†). The synthesis of the bulk La-MOF was confirmed by PXRD analysis, whereas the pattern of the as-synthesized La-MOF sample was in good agreement with that of Ce-MOF-589 (Fig. 2), suggesting that the La-MOF is reticular with the Ce-MOF-589 structure. Although the length of the La-MOF crystal was sufficient, its thickness and width were not satisfactory for single-crystal X-ray diffraction study. Therefore, the crystal structure of the La-MOF was instead determined by full profile matching Pawley refinement of powder X-ray diffraction (PXRD) data. In this respect, the crystal model of the La-MOF-589 structure was prebuilt by replacing the Ce^{3+} ion of Ce-MOF-589 (CCDC number 1843313) with a La^{3+} ion, and the Pawley refinement was accordingly performed (ESI,† Section S2).

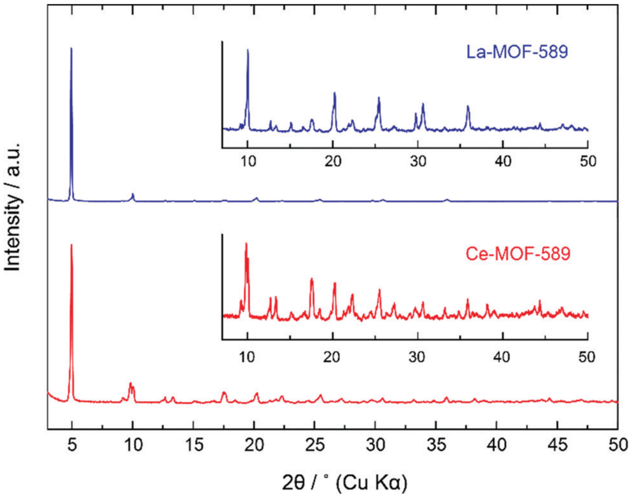

Fig. 2 Powder X-ray diffraction patterns of experimental La-MOF-589 (blue) and Ce-MOF-589 (red).

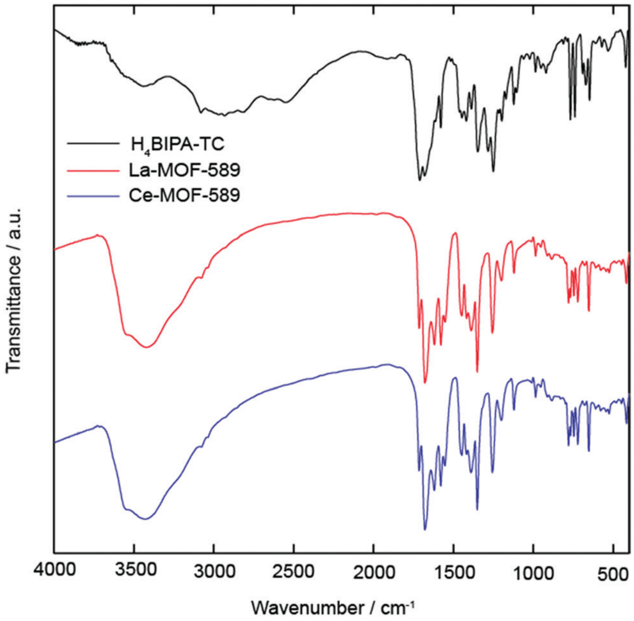

Fig. 3 FT-IR spectra of the H_4BIPA-TC linker (black), La-MOF-589 (red), and Ce-MOF-589 (blue).

As depicted in Fig. S3 (ESI†), there was a good match between the initial and the refined unit cell parameters of La-MOF-589. According to the structural refinement, La-MOF-589 crystallizes in the triclinic $P\bar{1}$ space group with unit cell parameters of a = 8.2030 Å, b = 11.0561 Å, and c = 17.4692 Å. Similar to Ce-MOF-589, the structure of La-MOF-589 is built up from dinuclear $[La_2(\text{-COO})_6(\text{-COOH})_2(H_2O)_6]$ units, which are interconnected by BIPA-TC ligands to form a parallelogram channel and window size of 5.5 × 10.4 Å^2 (Fig. 1A). In the two isostructural Ln-MOF-589 materials, the distance between two neighboring BIPA-TC units is approximately 3.0 Å, which could afford π–π interactions and improve the structural stability of the Ln-based frameworks (Fig. 1B).

To assess the successful synthesis of microcrystalline Ln-MOF-589, the PXRD analysis of the as-synthesized and activated Ln-MOF-589 samples was compared to that of the calculated patterns from the crystal structures. The as-synthesized Ln-MOF-589 materials were solvent-exchanged with dry EtOH, followed by vacuum activation at elevated temperatures to generate activated Ln-MOF-589 materials. As such, the PXRD patterns of the activated Ln-MOF-589 samples presented good agreement with those of the as-synthesized ones and those calculated from the crystal structures (Fig. S4 and S5, ESI†), indicating that the two Ln-MOFs retained their frameworks upon the activation process. Moreover, the FT-IR spectra of the Ln-MOFs showed identical characteristic peaks, suggesting the isostructural nature of the two Ln frameworks (Fig. 3). As shown in Fig. S7 (ESI†), FT-IR analysis of the dried Ln-MOF-589 showed sharp peaks at 1714 and 1678 cm^{-1} according to the amide carbonyl stretching vibrations. The two Ln-MOFs presented absorption bands at ∼1578 and 1447–1388 cm^{-1} corresponding to the antisymmetric and symmetric carbonyl COO^- vibrations. This evidence indicated the presence of the carboxylate group in the Ln-MOF-589 structures. Broad peaks at about 3436 cm^{-1} associated with the stretching modes of water molecules were also observed in the two frameworks. In comparison to the free H_4BIPA-TC ligand, the generation of additional sharp peaks at 1552 and 1618 cm^{-1} for La-MOF-589, and 1553 and 1619 cm^{-1} for Ce-MOF-589, assigned as asymmetric vibrations of the carboxylate group, suggested the emergence of metal–carboxylate coordination.

Thermogravimetric analyses of the Ln-MOF-589 frameworks were performed on activated MOF samples under an air-flow environment and a heating rate of 5 °C per minute (Fig. S8, ESI†). As shown in Fig. S8 (ESI†), the TGA curves exhibited insignificant weight loss in the temperature range from 25 to 150 °C, corresponding to the loss of guest water molecules. The major weight loss observed at 400 and 350 °C for La-MOF-589 and Ce-MOF-589, respectively, was attributed to framework destruction (Fig. S8, ESI†). Analyses of the weight percent of residual metal oxide for La-MOF-589 (21.54%) and Ce-MOF-589 (22.05%) exhibited good agreement with the calculated values derived from EA (21.77 and 21.88%, respectively).

The permanent porosity of the activated Ln-MOF-589 frameworks was evaluated by collecting N_2 sorption isotherms at 77 K. As illustrated in Fig. 4A, the two Ln-MOF-589 materials exhibited a type-I sorption profile, demonstrating that Ln-MOF-589 possesses a feature of micropore structure. Furthermore, the isotherms of the two Ln-MOF-589 frameworks revealed moderate hysteresis at the high-pressure region ($P/P_0 > 0.45$), indicating framework flexibility or guest molecule rearrangement. The Brunauer–Emmett–Teller (BET)/Langmuir surface areas for La-MOF-589 and Ce-MOF-589 were estimated to be 12/13 and 16/25 m^2 g^{-1}, respectively. From the N_2 isotherms, the pore size distributions of the two Ln-MOFs were calculated by fitting nonlocal density functional theory models. As expected, the calculated values were in line with the pore aperture metrics derived from the crystal structures (Fig. 4A).

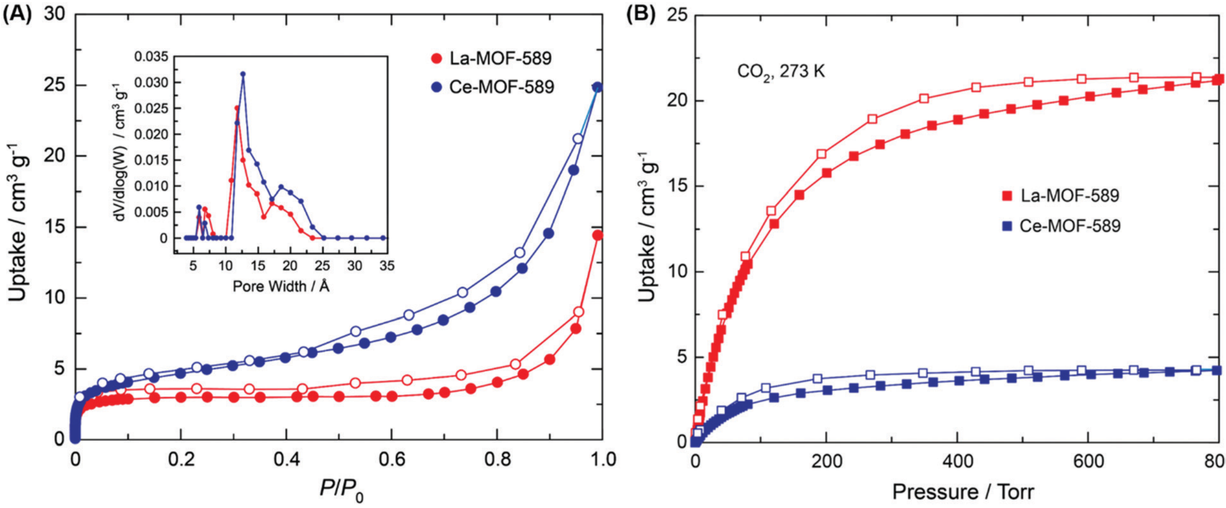

Fig. 4 (A) N_2 sorption isotherms at 77 K, (inset) pore size distribution analyses based on the DFT method, and (B) CO_2 sorption isotherms at 273 K for La-MOF-589 (red) and Ce-MOF-589 (blue).

The CO_2 sorption isotherms at 273 K for the two Ln-MOFs had typical type I shapes with small degrees of adsorption/desorption hysteresis (Fig. 4B). At 800 Torr, the total CO_2 uptake of La-MOF-589 (21.3 cm^3 g^{-1}) was higher than that of Ce-MOF-589 (4.2 cm^3 g^{-1}). Notably, the La-based framework also exhibited a broader extension of hysteresis than the Ce-based framework, suggesting different interactions between each Ln-MOF-589 framework and CO_2. When raising the activation temperature for La-MOF-589 and Ce-MOF-589 to 90 °C, the total CO_2 uptake for the two Ln-MOF-589 compounds was lower than that of the frameworks activated at 60 °C (Fig. S9 and S10, ESI†). It can be explained by the fact that water molecules that coordinate to open-Ln sites and are retained inside the MOF's pores could afford weak coordination to CO_2 induced by the quadrupole moment of CO_2 and the electric field created by water molecules, thus increasing the total CO_2 uptake.[38] A broad hysteresis loop of La-MOF-589 was also noted, which indicated that the adsorbed CO_2 was trapped within the framework and not desorbed immediately upon reducing the external pressure. It is worth noting that the La and Ce-based frameworks have a similar surface area and the same structure but showed different CO_2 sorption behaviours. This result was attributed to the different Ln-based metals, which afforded different interactions with CO_2.

Catalytic studies

In the Ln-MOF-589 (Ln = La, Ce) structures, the Ln clusters have large coordination with water molecules, which can afford accessible Lewis and Brønsted acid sites. By taking advantage of the high density of catalytic acid sites and the intrinsic nature of the electron-rich naphthalene diimide core, the Ln-MOF-589 materials were efficient platforms for the catalytic oxidation reaction. To achieve the optimized reaction conditions, we first used the Ce-MOF-589 framework as a model platform to investigate the impacts of solvent type, temperature, catalyst amount, oxidant type, and oxidant ratios.

The type of solvent has an effect in the catalytic oxidation of olefins. Highly polar alkylamine solvents (*e.g.*, DMF and acetonitrile) exhibit high activity in the oxidation reaction.[39] In our work, we initially examined the effect of the solvent (5 mL) on the catalytic oxidation of styrene catalyzed by Ce-MOF-589 by employing non-polar (*i.e.*, toluene) and polar (*i.e.*, ethanol and acetonitrile) solvents in the model reaction. Among the examined solvents, ethanol showed the lowest conversion of styrene (20%) and the highest selectivity in styrene oxide formation (73%) (Fig. 5). In contrast, acetonitrile displayed the highest conversion (64%) and the lowest selectivity in styrene oxide production (63%). The non-polar toluene solvent exhibited a lower yield of styrene oxide (34%) than the polar acetonitrile solvent (41%). Notably, the solvent-free condition

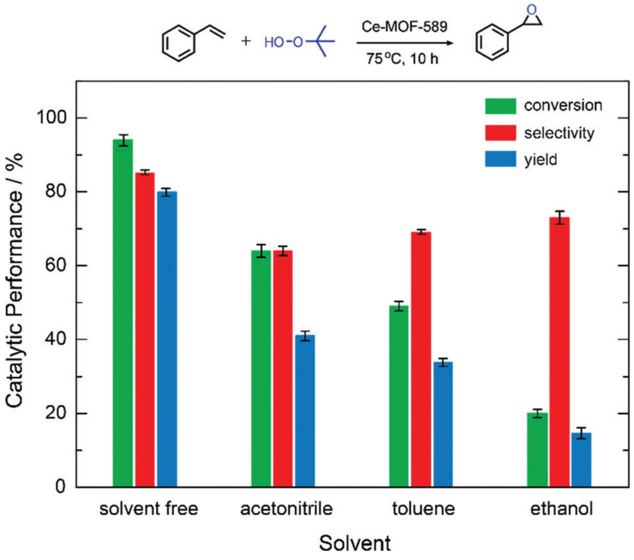

Fig. 5 Catalytic performances in styrene oxidation catalyzed by Ce-MOF-589 in different solvents. Error bars indicate the range of data based on three repeat experiments.

revealed the best catalytic performance with a conversion of 94% and a yield of styrene oxide of 80% for 10 h.

The effect of temperature on the oxidation of styrene was accordingly examined in the range of 25–85 °C (Fig. 6). Notably, the reaction performed at room temperature showed neither conversion of styrene nor styrene oxide formation after 10 h. At 65 °C, the oxidation exhibited a moderate performance with 72% conversion of styrene and a 52% yield of styrene oxide. When the reaction temperature increased from 65 to 75 °C, the conversion of styrene increased correspondingly (from 72 to 94%), resulting in a high yield of styrene oxide (80%) at 75 °C. Further increasing the temperature to 85 °C, no considerable variation in the conversion of styrene (95%) was observed, but the selectivity and yield of styrene epoxide slightly dropped to 66 and 70%, respectively. We proposed that the decrease of the styrene oxide selectivity was associated with the increase of the temperature, suggesting that the vinyl C–H bonds of styrene molecules are very active and readily oxidized to other products at high temperature.[40] Therefore, 75 °C was chosen as the control temperature for further studies.

Subsequently, the effect of the catalyst amount on the oxidation reaction was investigated by carrying out the reaction with 0, 0.3, 0.5, 0.7, and 0.9 mol% (calculated based on metal sites) of the Ce-MOF-589 catalyst (Fig. 7). We noted that the blank reaction without the MOF catalyst presented the lowest performance with a 28% conversion of styrene and an 18% yield of styrene oxide. When the catalyst amount increased from 0.3 to 0.7 mol%, the conversion of styrene and selectivity of styrene oxide dramatically increased with rises of 44 and 39%, respectively. However, a further increase of the MOF amount to 0.9 mol% was ineffective and instead resulted in lower selectivity (80%) and yield (76%) of styrene oxide. This result indicated that the assessment of sufficient catalyst affords a more accessible surface area with a high distribution of active sites, resulting in enhancing the styrene oxidation rate. In contrast, overuse of MOF catalysts could block the active sites and reduce the solid–liquid interactions between catalysts and reactants, yielding lower catalytic activity. Thus, a catalyst loading of 0.7 mol% was the optimized value for obtaining the highest catalytic performance.

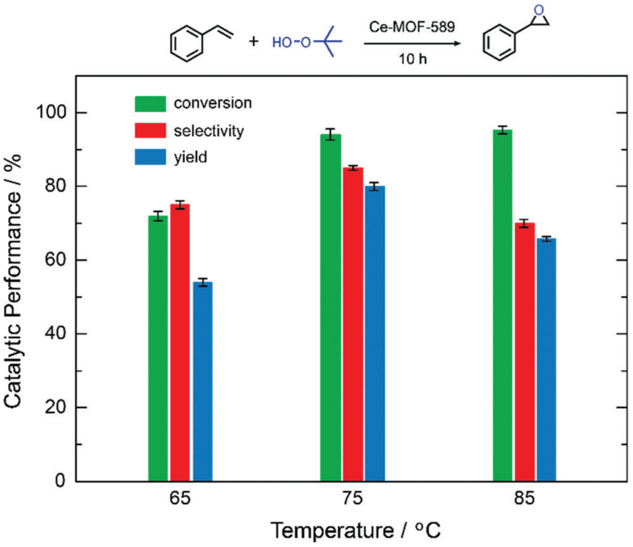

Fig. 6 Catalytic performances in styrene oxidation catalyzed by Ce-MOF-589 at different temperatures. Error bars indicate the range of data based on three repeat experiments.

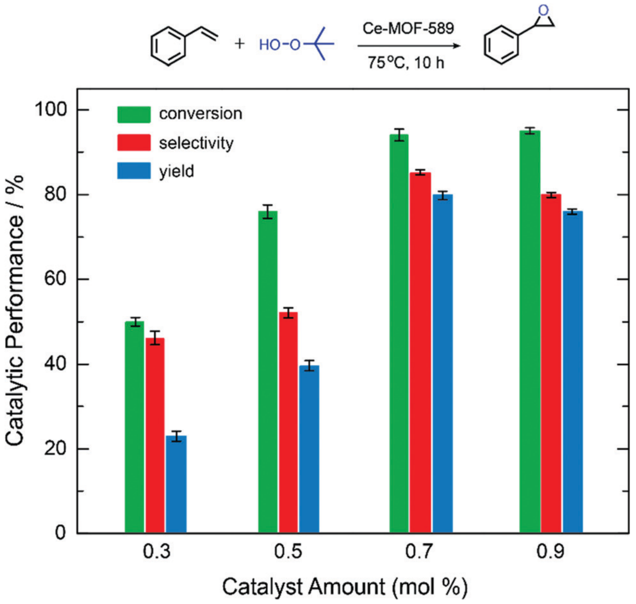

Fig. 7 Catalytic performances in styrene oxidation catalyzed by Ce-MOF-589 at different amounts of MOF catalyst. Error bars indicate the range of data based on three repeat experiments.

The oxidant type also exhibited an influence on the oxidation of styrene catalyzed by Ce-MOF-589. Different oxidants such as H_2O_2, $NaIO_4$, and aqueous TBHP (70% in water) were employed in the catalytic oxidation of styrene. As depicted in Fig. 8, the media using H_2O_2 and $NaIO_4$ exhibited the lowest activities among the oxidants examined with styrene oxide yields of 1% and 2%, respectively. Otherwise, aqueous TBHP showed moderate catalytic performance with a styrene conversion of 70% and styrene oxide yield of 45%. Notably, the oxidation promoted by anhydrous TBHP (TBHP in decane) exhibited the highest efficiency with a conversion of 94% and a yield of styrene oxide of 80%.

The effect of the styrene/TBHP molar ratio on the generation of styrene oxide was consequently studied by conducting the reaction at different molar ratios of 1 : 1, 1 : 2, and 1 : 3. Moderate catalytic performance with a conversion of 60% and selectivity of 53% was observed at a molar ratio of 1 : 1, associated with lower availability of active oxidant to interact with the substrate. When the molar ratio increased to 1 : 2, the conversion of styrene and the selectivity of styrene oxide formation increased to 94 and 85%, respectively (Fig. 9). It was attributed to the higher amount of TBHP adsorbed on the active sites, thereby leading to more interaction with styrene molecules. When the styrene/TBHP molar ratio reached 1 : 3, the conversion of styrene slightly increased, but the selectivity and yield of styrene oxide gradually decreased. We noted that an excess amount of TBHP could improve the

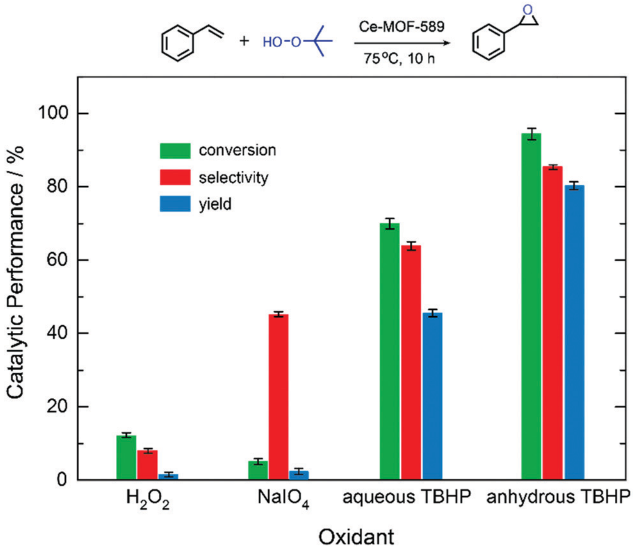

Fig. 8 Catalytic performances in styrene oxidation catalyzed by Ce-MOF-589 in different oxidants. Error bars indicate the range of data based on three repeat experiments.

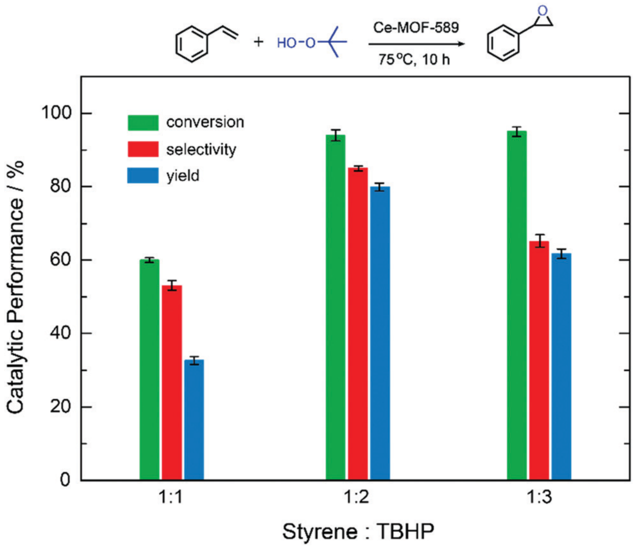

Fig. 9 Catalytic performances in styrene oxidation catalyzed by Ce-MOF-589 for different molar ratios of styrene and TBHP. Error bars indicate the range of data based on three repeat experiments.

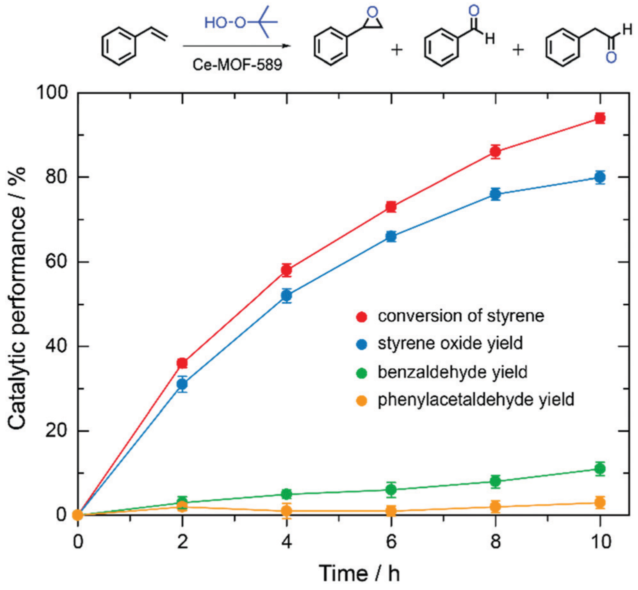

Fig. 10 Oxidation product distribution at different reaction times. Error bars indicate the range of data based on three repeat experiments.

conversion of styrene and also facilitate the oxidation of styrene oxide to benzaldehyde and phenylacetaldehyde. From this viewpoint, a styrene/TBHP ratio of 1 : 2 exhibited the best activity among the examined conditions.

To gain insight into the oxidation reaction, the product distribution at different reaction times was investigated (Fig. 10). Under an N_2 environment, the conversion of styrene reached 36% after 2 h and obtained a maximized value of 94% for 10 h. Because of no significant increase in the conversion of styrene and a slight decrease in the yield of styrene oxide, further increasing the reaction time after 10 h was found to be ineffective. At the early stage of the reaction, the formation of styrene oxide increased rapidly (a rise of 32%) with the presence of trace amounts of benzaldehyde and phenylacetaldehyde by-products. Low selectivity and yield of these by-products were observed within 8 h and they slightly increased at prolonged reaction time. Interestingly, high selectivities (85–90%) in styrene oxide formation were noted during the oxidation of styrene catalyzed by Ce-MOF-589.

With the optimized conditions, the catalytic activity in the epoxidation of styrene for La-MOF-589 was accordingly examined (Table 1). As such, La-MOF-589 exhibited lower catalytic performance (a conversion of 60%, selectivity of 78%, and yield of 47%) compared to Ce-MOF-589 (a conversion of 94%, selectivity of 85%, and yield of 80%). Benzaldehyde and phenylacetaldehyde were also found to be by-products and occurred in trace amounts during the oxidation reaction catalyzed by La-MOF-589. We noticed that the two Ln-MOF-589 materials are isostructural and have similar aperture sizes, but the Ce-based framework exhibited higher activity than the

Table 1 Catalytic styrene oxidation catalyzed by Ln-MOF-589[a]

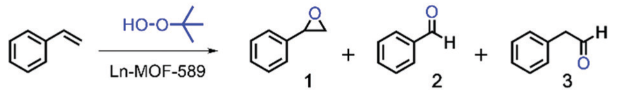

Catalyst	Conversion[b]/%	Selectivity[b]/% 1	2	3	Yield[b]/%
La-MOF-589	60	78	41	12	47
Ce-MOF-589	94	85	12	3	80
No catalyst	28	64	26	10	18

[a] Reaction conditions: styrene (5 mmol), catalyst (0.7 mol%, based on metal sites), TBHP (10 mmol), 75 °C, 10 h. [b] The conversion, selectivity, and yield of the main product (styrene oxide) were determined by GC-FID analysis using chlorobenzene as the internal standard. **1** = styrene oxide, **2** = benzaldehyde, and **3** = phenylacetaldehyde.

La-based structure. It could be explained by the easy formation of the stable (+IV) oxidation state of the Ce ion according to its vacant f-shell.

The catalytic activities of the Ln-MOF-589 frameworks for the epoxidation of styrene were comparable with those of some of the homogenous and heterogeneous catalysts, and MOFs reported before (Table 2). Accordingly, homogenous Ce salts $Ce(NO_3)_3{\cdot}6H_2O$ and $[Ce(NO_3)_6](NH_4)_2$ showed high conversions of styrene (84 and 98%, respectively) but low selectivities of styrene oxide (3%). Among homogenous Ln salts, $La(NO_3)_3{\cdot}6H_2O$ exhibited poor performance with moderate conversion (54%) and the lowest selectivity of epoxide (2%), compared to that of $La(CH_3COO)_3{\cdot}xH_2O$ (41% conversion and 81% selectivity). Moreover, a catalytic reaction using the H_4BIPA-TC linker showed moderate performance with 25% conversion of styrene and only a 14% yield of styrene oxide. Furthermore, oxidation reactions catalyzed by mixtures of $La(NO_3)_3{\cdot}6H_2O/H_4$BIPA-TC and $Ce(NO_3)_3{\cdot}6H_2O/H_4$BIPA-TC resulted in moderate conversions of styrene (62 and 86%, respectively) and low selectivities of styrene oxide formation (38 and 43%, respectively). This evidence supported the high catalytic activity of the Ce-MOF-589 framework constructed from Ce-based clusters and the naphthalene diimide linker. Moreover, heterogeneous La_2O_3 and CeO_4 solids facilitated low efficiencies with styrene oxide yields of 19 and 31%, respectively. Interestingly, Ce-MOF-589 exhibited a higher activity than representative MOFs with larger surface areas such as HKUST-1, ZIF-8, MIL-53, MOF-177, and Ce-MOF-76. Among these comparative MOFs, MIL-53 revealed the lowest catalytic activity, reaching only a 6% yield of styrene oxide, while Ce-MOF-76 was the most active with a 46% yield achieved. By comparing these results, it is worth noting that high surface area and high total CO_2 uptake at room temperature are not the most decisive factors for catalytic epoxidation. This evidence supports the exceptional performance of Ce-MOF-589 and the synergic effect of Lewis acid $[Ce_2(\text{-}COO)_6(\text{-}COOH)_2(H_2O)_6]$ units and the naphthalene diimide-based linker within Ce-MOF-589 for the catalytic oxidation reaction.

Table 2 Comparison of the catalytic performance of representative catalysts[a]

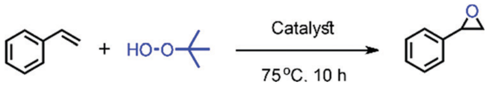

#	Type	Catalyst	Con.[b]/%	Sel.[b]/%	Yie.[b]/%
1	Hom.	$La(NO_3)_3{\cdot}6H_2O$	54	2	1
2		$La(CH_3COO)_3{\cdot}xH_2O$	41	81	33
3		$Ce(NO_3)_3{\cdot}6H_2O$	84	3	2
4		$[Ce(NO_3)_6](NH_4)_2$	98	3	3
5		H_4BIPA-TC linker	25	56	14
6		$La(NO_3)_3{\cdot}6H_2O$ + H_4BIPA-TC	62	38	24
7		$Ce(NO_3)_3{\cdot}6H_2O$ + H_4BIPA-TC	86	43	37
8	Het.	La_2O_3	40	48	19
9		CeO_4	52	60	31
10	MOF	La-MOF-589	60	78	47
11		Ce-MOF-589	94	85	80
12		ZIF-8	86	54	47
13		HKUST-1	90	48	43
14		MIL-53	67	8	6
15		MOF-177	34	32	11
16		Ce-MOF-76	85	54	46

[a] Reaction conditions: styrene (5 mmol), catalyst (0.7 mol%, based on metal sites), TBHP (10 mmol), 75 °C, 10 h. [b] Conversion (Con.), selectivity (Sel.), and yield (Yie.) were determined by GC-FID analysis using chlorobenzene as the internal standard. Hom. = homogeneous, and Het. = heterogeneous.

Encouraged by the above results, we further investigated the oxidation of cyclohexene catalyzed by two Ln-based frameworks (Table 3). We noted that the blank reaction without any catalyst gave a negligible conversion (30%) and a low yield of 2-cyclohexen-1-one (17%). Under the optimum conditions, 2-cyclohexen-1-one and cyclohexene-3-(*tert*-butyl)peroxide were obtained as major products, and only a trace amount of cyclohexene epoxide and 2-cyclohexen-1-ol was detected. As shown in Table 3, Ce-MOF-589 exhibited outstanding performance with a high conversion of cyclohexene (90%) and a high yield of 2-cyclohexen-1-one (85%). In contrast, La-MOF-589 showed a moderate transformation of cyclohexene to 2-cyclohexen-1-one (a conversion of 54% and yield of 49%). Remarkably, the two Ln-MOF-589 frameworks exhibited excellent catalytic selectivities for 2-cyclohexen-1-one formation (90–95%). It is worth noting that the cyclohexene oxidations catalyzed by the two Ln-based structures were highly selective towards the 2-cyclohexen-1-one product in the model experiment because the allylic hydrogen is generally more reactive than the double bond of the cyclic fragment.

A leaching experiment was performed to verify the heterogeneity of the reaction (Fig. 11). The Ce-MOF-589 catalyst was isolated at 4 h and the supernatant reaction was allowed to proceed for an additional 6 h under similar conditions. As shown in Fig. 11, no significant increase in styrene oxide formation was observed. The result confirmed the heterogeneity of the catalytic oxidation reaction, and the contribution of homogeneous Ce^{3+} leaching from the Ce-MOF-589 structure to the generation of styrene oxide was unimportant. Furthermore, ICP-MS of the reaction filtrate demonstrated that a trace amount of Ce^{3+} ions was observed (<0.085 ppm), confirming the structural stability of Ce-MOF-589 upon catalytic oxidation.

Table 3 Catalytic cyclohexene oxidation catalyzed by Ln-MOF-589[a]

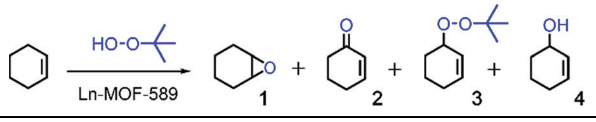

Catalyst	Conversion[b]/%	Selectivity[b]/% 1	2	3+4	Yield[b]/%
La-MOF-589	54	4	90	6	49
Ce-MOF-589	90	2	95	3	85
No catalyst	30	16	58	26	17

[a] Reaction conditions: cyclohexene (5 mmol), catalyst (0.7 mol%, based on metal sites), TBHP (10 mmol), 75 °C, 10 h. [b] The conversion (Con.), selectivity (Sel.), and yield of the main product (Yie.) were determined by GC-FID analysis using chlorobenzene as the internal standard. **1** = cyclohexene oxide, **2** = 2-cyclohexen-1-one, and **3**+**4** = cyclohexene-3-(*tert*-butyl)peroxide + 2-cyclohexen-1-ol.

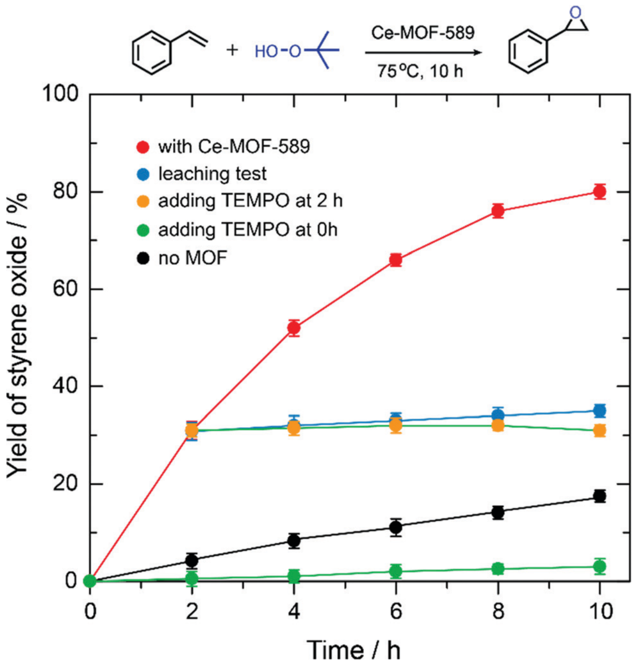

Fig. 11 Time dependent yield of styrene oxide in leaching, TEMPO, and no-MOF experiments. Error bars indicate the range of data based on three repeat experiments.

Subsequently, the reusability of the Ce-MOF-589 catalyst for the oxidation of styrene was examined under the optimized reaction conditions (Fig. 12). Remarkably, Ce-MOF-589 was recovered and reused up to six times without any significant decrease in catalytic activity, which was demonstrated by the reasonable average values of conversion (92%), selectivity (79%), and yield (73%) of styrene oxide. Furthermore, the PXRD and FT-IR analyses of the reused Ce-MOF-589 catalyst showed no significant change in the peak intensity and position (ESI,† Fig. S21 and S22), implying that the Ce-based framework retained its structural integrity after several catalytic reactions. As depicted in Fig. S23 (ESI†), the SEM image of Ce-MOF-589 after the 6th cycle also confirmed that Ce-MOF-589 maintained its particle morphology over several catalytic reactions. We also found that the yellow color of the large-scale Ce-MOF-589 solid was unchanged after several catalytic reactions, as illustrated in Fig. S24 (ESI†).

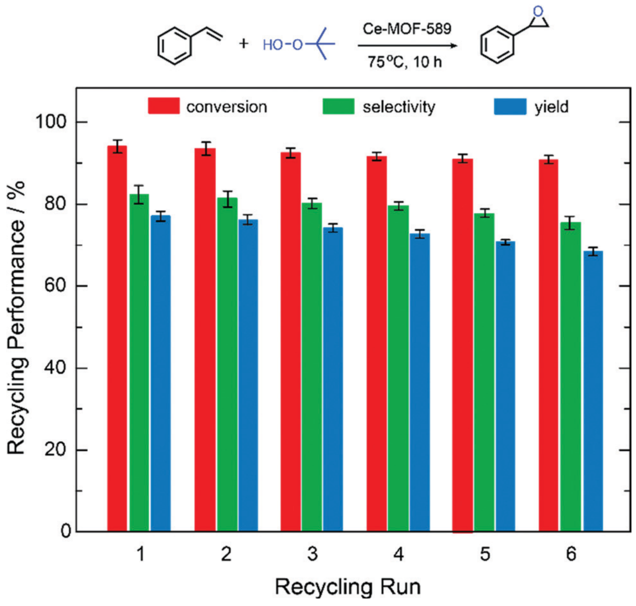

Fig. 12 Recycling study for Ce-MOF-589. Error bars indicate the range of data based on three repeat experiments.

Reaction mechanism

Because of the narrow aperture size of Ce-MOF-589 (5.6 × 11.4 Å^2), the activation of Ce^{3+} by the TBHP (*t*-BuOOH) oxidant generally occurred on the external surface of Ce-MOF-589. Through the interaction with *t*-BuOOH, Ce(III)-MOF-589 transformed to Ce(IV)-MOF-589 owing to the presence of a vacant f-shell (the electron configuration of Ce^{3+} is [Xe]4f^{1}5d^{0}6s^0). Therefore, the catalytic activity of Ce-MOF-589 is higher compared to La-MOF-589, due to the lack of a vacant f-shell (the electron configuration of La^{3+} is [Xe]5d^{0}6s^0).

To confirm the oxidation state of the Ce ion within Ce-MOF-589, XPS was performed on the activated Ce-MOF-589 sample. As depicted in Fig. 13, the Ce 3d core-level spectrum revealed the presence of v and u multiplets assigned to spin–orbit split 3d$_{5/2}$ and 3d$_{3/2}$ core holes, respectively.[41–44] Three peaks of binding energies at 880.1, 884.1, and 903.3 eV corresponding to v$_0$, v′, and u′, respectively, were ascribed to be characteristics of Ce^{3+}. Otherwise, three peaks attributed to Ce^{4+}, whose binding energies were at 883.5, 898.6, and 901.9 eV, labeled as v, v″, and u, respectively, were also observed. This result suggested that the activated Ce-MOF-589 is possibly composed of a mixed-valence state of Ce^{3+} and Ce^{4+}. From the integrated peak area, the relative amount of Ce^{3+} was accordingly estimated to be 83%. This observation indicated that the Ce-MOF-589 framework contains mostly Ce^{3+}. We supposed that the presence of Ce^{4+} in the activated Ce-MOF-589 sample could be attributed to

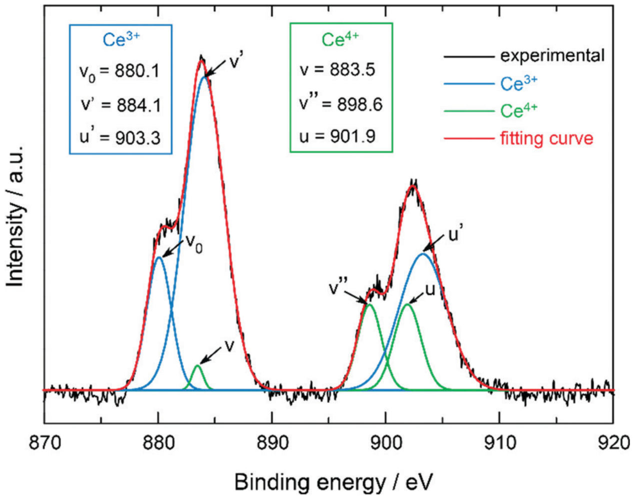

Fig. 13 XPS spectrum of the Ce 3d core level of the activated Ce-MOF-589.

the partial oxidization of Ce(III)-MOF to Ce(IV)-MOF under an air environment.

According to previous literature, different intermediates could be generated when the transition metal site interacts with *t*-BuOOH.[23,45–47] There are two major pathways involved: (i) the production of free radical intermediates such as *t*-BuOO• and/or *t*-BuO• radicals; and (ii) the concerted addition of oxygen, yielding high valent metal-peroxo and/or metal-oxo species. To ascertain the nature of styrene oxidation catalyzed by Ce-MOF-589, a radical scavenger, 2,2,6,6-tetramethylpiperidine-1-oxyl (TEMPO, 1 equiv. to the moles of TBHP used), was added into the medium at the beginning of the reaction. A trace amount of styrene oxide (yield of 3%) was observed after 10 h (Fig. 11). When TEMPO was added into the medium after 2 h (36% conversion obtained), the reaction stopped producing styrene oxide immediately (Fig. 11). Accordingly, a slight decrease in the yield of styrene oxide was observed after 8 h reaction time (Fig. 11). This result could be explained by the formation of phenylacetaldehyde and benzaldehyde from the consequent reactions of styrene oxide with Ce sites and styrene oxide with TBHP, respectively. All of the evidence suggested that the mechanism of the oxidation of styrene proceeded mainly *via* a radical process.[48,49]

Accordingly, the mechanism of styrene oxidation was proposed (Scheme 1). First, Ce(III)-MOF-589 reacts with *t*-BuOOH to form a Ce(IV)-peroxy adduct. Then, the Ce(IV)-peroxy adduct releases the *t*-BuOO• radical, and Ce(III)-MOF is regenerated. It is followed by a reaction between the *t*-BuOO• radical and olefin, forming a benzylic *t*-butylperoxy radical. The benzylic *t*-butyl peroxy radical either (i) undergoes migration of oxygen, yielding the styrene oxide and *t*-BuOH (Scheme 1, route I); or (ii) reacts with *t*-BuOO•, producing benzaldehyde *via* oxidative C–C bond cleavage (Scheme 1, route II).

A ring-opening of styrene oxide with *t*-BuOOH followed by C–C cleavage could occur, resulting in benzaldehyde. Moreover, the benzylic *t*-butylperoxy radical can undergo the migration of hydrogen to a benzylic carbon and simultaneous cleavage of O–O (Scheme 1, route III), resulting in phenylacetaldehyde and *t*-BuOH. Otherwise, the Lewis-acid Ce(III) sites can induce a ring-opening isomerization of styrene oxide, which involves hydride migration and the regeneration of active Ce(III) sites, affording phenylacetaldehyde.[50,51] These proposed pathways confirmed the experimental result indicating that the higher the amounts of *t*-BuOOH or Ce-MOF-589 catalyst compared to those of the optimized conditions used, the lower the selectivities and yields of styrene oxide achieved. That is due to the consequent reactions between the resulting styrene oxide and the excess *t*-BuOOH and/or Ce-MOF-589.

As for the oxidation of cyclohexene, there was no significant change in the conversion of cyclohexene and yield of

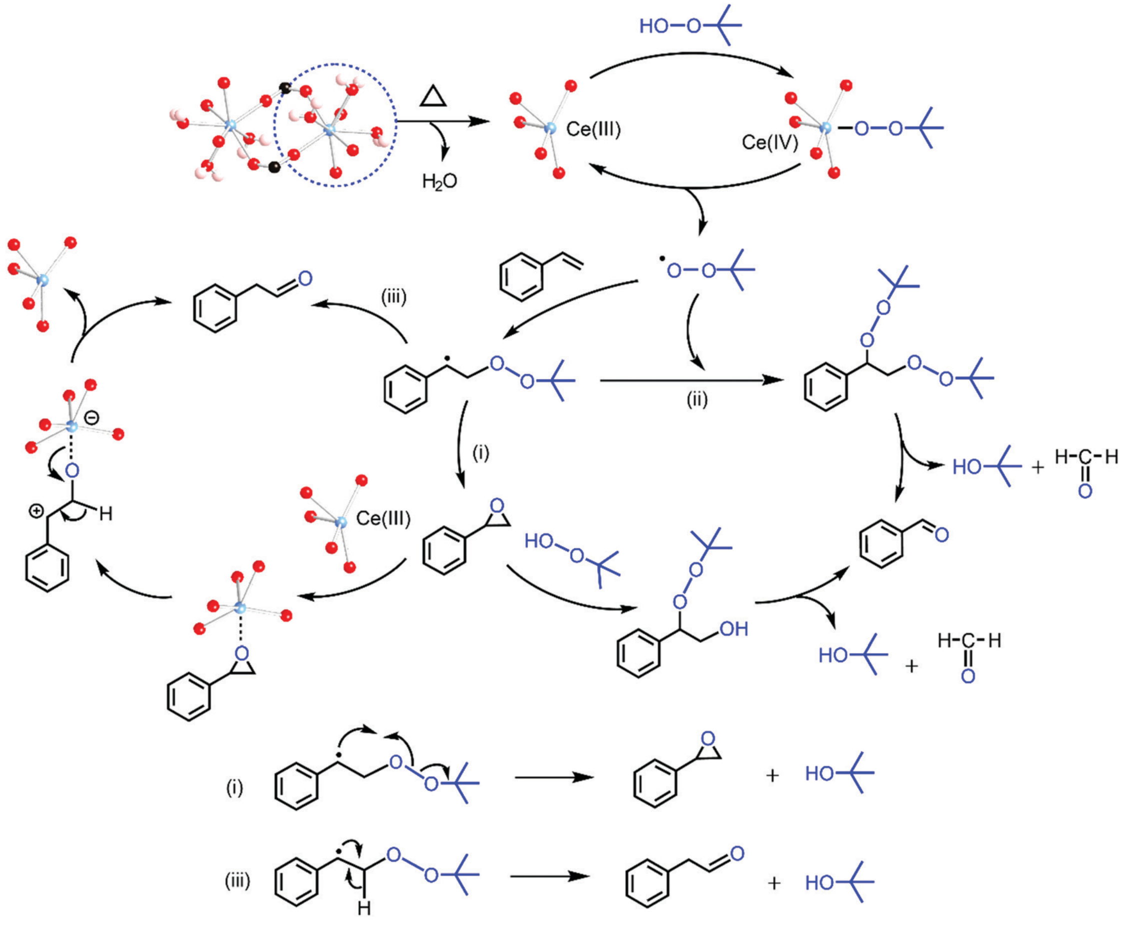

Scheme 1 Possible mechanism for the oxidation of styrene catalyzed by Ce-MOF-589.

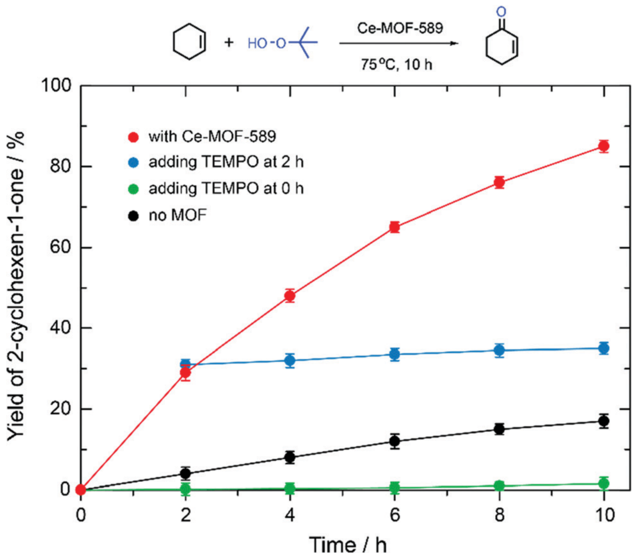

Fig. 14 Time dependent yield of 2-cyclohexen-1-one in TEMPO and no-MOF experiments. Error bars indicate the range of data based on three repeat experiments.

2-cyclohexen-1-one when TEMPO was inserted into the media at the beginning and 2 h reaction time (Fig. 14). As shown in Fig. 14, 2-cyclohexen-1-one and cyclohexene-3-(*tert*-butyl)peroxide were the major products while cyclohexene oxide existed as a minor product, suggesting the involvement of radical species in the cyclohexene oxidation process.[34,47,48,52] Cyclohexene has allylic hydrogen that is more active than the C=C bond toward the *t*-BuOO• and *t*-BuO• radicals, and thus the oxidation reaction afforded mainly allylic oxidation products. Based on our experimental results and previous reports, the mechanism of cyclohexene oxidation was proposed (Scheme 2).[47,53] First, *t*-BuOO• and *t*-BuO• radical species are produced from the interaction between TBHP and Ce(III) centers.[54] As illustrated in Scheme 2, route-I revealed hydrogen transfer from α-C-H of cyclohexene to *t*-BuO• and/or *t*-BuOO• radicals, resulting in cyclohexenyl radicals. Subsequently, the cyclohexenyl radical combines with the *t*-BuOO• radical to afford the cyclohexene-3-(-(*tert*-butyl)-peroxide) product.[55] Also, the cyclohexenyl radical could react with O_2, generated from the combination of two *t*-BuOO• radicals, to produce the cyclohexenyl peroxy radical. Accordingly, the cyclohexenyl peroxy radical undergoes an elimination reaction to form 2-cyclohexen-1-one and 2-cyclohexen-1-ol. Also, the *t*-BuOO• radical can combine with the C=C bond, yielding the cyclohexyl 2-peroxide radical. The intermediate accordingly undergoes ring-closing to produce cyclohexene oxide (Scheme 2, route II).[56]

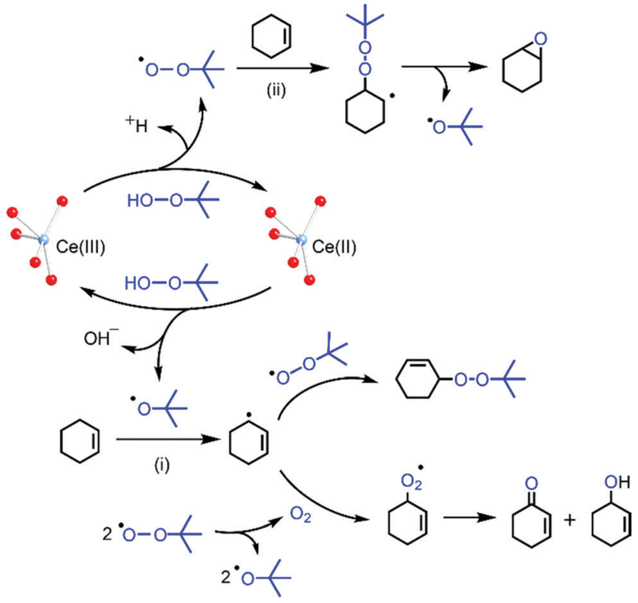

Scheme 2 Possible mechanism for the oxidation of cyclohexene catalyzed by Ce-MOF-589.

Conclusions

In summary, two isostructural lanthanide-based MOFs, namely Ln-MOF-589 (Ln = La, Ce), were synthesized and characterized. In this series, Ce-MOF-589 exhibited the higher surface area but lower total CO_2 uptake (at 298 K and 800 Torr), compared to those of Ln-MOF-589. As for the catalytic oxidation, Ce-MOF-589 exhibited the highest catalytic conversions of styrene (94%) and cyclohexene (90%) by using anhydrous TBHP oxidant, and under mild conditions (solvent-free, 75 °C, N_2 atmosphere, 10 h). Styrene, a terminal olefin with no allylic hydrogen, provided 85% selectivity and 80% yield for the styrene oxide product. In contrast, cyclohexene, which possesses allylic hydrogen, resulted in high total yields (>85%) of the allylic oxidation products of 2-cyclohexen-1-one and cyclohexene-3-(*tert*-butyl)peroxide. Our experimental results also showed that a free radical mechanism is the main pathway for the oxidation of olefins catalyzed by Ln-MOF-589 (Ln = La, Ce) frameworks.

Author contributions

Y. B. N. Tran: Validation, Formal analysis, Investigation, Data curation, Writing – original draft. Phuong T. K. Nguyen: Conceptualization, Methodology, Writing – original draft, Writing – review & editing, Visualization, Supervision.

Conflicts of interest

There are no conflicts to declare.

Acknowledgements

We are grateful to Provost. Dr Bao N. Le and Dr Ai. V. Dao (Duy Tan University) for supporting our science activities. We thank Dr Sunhwa Lee (Sungkyunkwan University) for her assistance with XPS analysis.

Notes and references

1 Y. Shi, in *Modern Oxidation Methods*, ed. J.-E. Bäckvall, Wiley-VCH, Weinheim, Second Edition, 2010, ch. 3, pp. 85–115.

2 P. C. B. Page and T. J. McCarthy, *Comprehensive Organic Synthesis*, Pergamon, Oxford, 1991.

3 A. Corma and H. García, *Chem. Rev.*, 2002, **102**, 3837–3892.

4 S. Linic and M. A. Barteau, in *Handbook of Heterogeneous Catalysis*, ed. G. Ertl, H. Knözinger, F. Schüth and J. Weitkamp, Wiley-VCH, Weinheim, 2008, pp. 3448–3464.

5 A. Dhakshinamoorthy, A. M. Asiri and H. Garcia, *Chem. – Eur. J.*, 2016, **22**, 8012–8024.

6 J. W. Maina, C. Pozo-Gonzalo, L. Kong, J. Schütz, M. Hill and L. F. Dumée, *Mater. Horiz.*, 2017, **4**, 345–361.

7 J. Gascon, A. Corma, F. Kapteijn and F. X. Llabrés i Xamena, *ACS Catal.*, 2014, **4**, 361–378.

8 C. Pagis, M. Ferbinteanu, G. Rothenberg and S. Tanase, *ACS Catal.*, 2016, 6063–6072.

9 A. Dhakshinamoorthy, M. Alvaro and H. Garcia, *Catal. Sci. Technol.*, 2011, **1**, 856–867.

10 H. Furukawa, K. E. Cordova, M. O'Keeffe and O. M. Yaghi, *Science*, 2013, **341**, 1230444.

11 P. T. K. Nguyen, H. T. D. Nguyen, H. N. Nguyen, C. A. Trickett, Q. T. Ton, E. Gutiérrez-Puebla, M. A. Monge, K. E. Cordova and F. Gándara, *ACS Appl. Mater. Interfaces*, 2018, **10**, 733–744.

12 J. Jiang, F. Gándara, Y.-B. Zhang, K. Na, O. M. Yaghi and W. G. Klemperer, *J. Am. Chem. Soc.*, 2014, **136**, 12844–12847.

13 J. Chen, Y. Li, J. Gu, M. V. Kirillova and A. M. Kirillov, *New J. Chem.*, 2020, **44**, 16082–16091.

14 Y. B. N. Tran, P. T. K. Nguyen, Q. T. Luong and K. D. Nguyen, *Inorg. Chem.*, 2020, **59**, 16747–16759.

15 A. Das, N. Anbu, P. Varalakshmi, A. Dhakshinamoorthy and S. Biswas, *New J. Chem.*, 2020, **44**, 10982–10988.

16 H. Li, K. Wang, D. Feng, Y.-P. Chen, W. Verdegaal and H.-C. Zhou, *ChemSusChem*, 2016, **9**, 2832–2840.

17 K. Leus, Y.-Y. Liu and P. Van Der Voort, *Catal. Rev.*, 2014, **56**, 1–56.

18 J. Jacobsen, A. Ienco, R. D'Amato, F. Costantino and N. Stock, *Dalton Trans.*, 2020, **49**, 16551–16586.

19 P. Cancino, L. Santibañez, C. Stevens, P. Fuentealba, N. Audebrand, D. Aravena, J. Torres, S. Martinez, C. Kremer and E. Spodine, *New J. Chem.*, 2019, **43**, 11057–11064.

20 P. Cancino, V. Paredes-García, C. Aliaga, P. Aguirre, D. Aravena and E. Spodine, *Catal. Sci. Technol.*, 2017, **7**, 231–242.

21 R. Sen, S. Koner, D. K. Hazra, M. Helliwell and M. Mukherjee, *Eur. J. Inorg. Chem.*, 2011, 241–248.

22 R. Dalapati, B. Sakthivel, A. Dhakshinamoorthy, A. Buragohain, A. Bhunia, C. Janiak and S. Biswas, *CrystEngComm*, 2016, **18**, 7855–7864.

23 P. Cancino, V. Paredes-García, P. Aguirre and E. Spodine, *Catal. Sci. Technol.*, 2014, **4**, 2599–2607.

24 L. Fan, K. Wang, K. Xu, Z. Liang, H. Wang, S.-F. Zhou and G. Zhan, *Small*, 2020, **16**, 2003597.

25 Z. Huang, F. Zhao, L. Fan, W. Zhao, B. Chen, X. Chen, S.-F. Zhou, J. Xiao and G. Zhan, *Mater. Des.*, 2020, **194**, 108881.

26 H. N. Abdelhamid, G. A.-E. Mahmoud and W. Sharmouk, *J. Mater. Chem. B*, 2020, **8**, 7548–7556.

27 H. N. Abdelhamid, M. Wilk-Kozubek, A. M. El-Zohry, A. Bermejo Gómez, A. Valiente, B. Martín-Matute, A.-V. Mudring and X. Zou, *Microporous Mesoporous Mater.*, 2019, **279**, 400–406.

28 H. N. Abdelhamid, A. Bermejo-Gómez, B. Martín-Matute and X. Zou, *Microchim. Acta*, 2017, **184**, 3363–3371.

29 K. Müller-Buschbaum, *The Chemistry of Metal–Organic Frameworks*, Wiley-VCH Verlag GmbH & Co., KGaA, 2016, ch. 9, pp. 231–270.

30 H. T. D. Nguyen, Y. B. N. Tran, H. N. Nguyen, T. C. Nguyen, F. Gándara and P. T. K. Nguyen, *Inorg. Chem.*, 2018, **57**, 13772–13782.

31 P. Cancino, A. Vega, A. Santiago-Portillo, S. Navalon, M. Alvaro, P. Aguirre, E. Spodine and H. García, *Catal. Sci. Technol.*, 2016, **6**, 3727–3736.

32 R. Sen, D. Saha and S. Koner, *Catal. Lett.*, 2012, **142**, 124–130.

33 R. Sen, D. K. Hazra, M. Mukherjee and S. Koner, *Eur. J. Inorg. Chem.*, 2011, 2826–2831.

34 A. Dhakshinamoorthy, M. Alvaro and H. Garcia, *ACS Catal.*, 2011, **1**, 836–840.

35 M. Tonigold, Y. Lu, A. Mavrandonakis, A. Puls, R. Staudt, J. Möllmer, J. Sauer and D. Volkmer, *Chem. – Eur. J.*, 2011, **17**, 8671–8695.

36 G. H. Dang, Y. B. N. Tran, T. V. Pham, V. T. Pham, N. T. H. Luu, H. D. Nguyen, P. T. K. Nguyen, H. T. D. Nguyen and T. Truong, *ChemPlusChem*, 2019, **84**, 1046–1051.

37 M. Al Kobaisi, S. V. Bhosale, K. Latham, A. M. Raynor and S. V. Bhosale, *Chem. Rev.*, 2016, **116**, 11685–11796.

38 A. Ö. Yazaydın, A. I. Benin, S. A. Faheem, P. Jakubczak, J. J. Low, R. R. Willis and R. Q. Snurr, *Chem. Mater.*, 2009, **21**, 1425–1430.

39 J.-H. Noh, R. Patala and R. Meijboom, *Appl. Catal., A*, 2016, **514**, 253–266.

40 S. Sharma, S. Sinha and S. Chand, *Ind. Eng. Chem. Res.*, 2012, **51**, 8806–8814.

41 C. Anandan and P. Bera, *Appl. Surf. Sci.*, 2013, **283**, 297–303.

42 R. Dalapati, B. Sakthivel, M. K. Ghosalya, A. Dhakshinamoorthy and S. Biswas, *CrystEngComm*, 2017, **19**, 5915–5925.

43 D. Yue, D. Zhao, J. Zhang, L. Zhang, K. Jiang, X. Zhang, Y. Cui, Y. Yang, B. Chen and G. Qian, *Chem. Commun.*, 2017, **53**, 11221–11224.

44 J. Wu, J. Liang, R. Ma and T. Sasaki, *J. Phys. Chem. C*, 2015, **119**, 26229–26236.

45 J. Zhang, A. V. Biradar, S. Pramanik, T. J. Emge, T. Asefa and J. Li, *Chem. Commun.*, 2012, **48**, 6541–6543.

46 M. Yonemitsu, Y. Tanaka and M. Iwamoto, *J. Catal.*, 1998, **178**, 207–213.

47 R. Antony, G. L. Tembe, M. Ravindranathan and R. N. Ram, *J. Mol. Catal. A: Chem.*, 2001, **171**, 159–168.

48 W.-J. Sun and E.-Q. Gao, *Mol. Catal.*, 2020, **482**, 110746.

49 H.-F. Yao, Y. Yang, H. Liu, F.-G. Xi and E.-Q. Gao, *J. Mol. Catal. A: Chem.*, 2014, **394**, 57–65.

50 R. Srirambalaji, S. Hong, R. Natarajan, M. Yoon, R. Hota, Y. Kim, Y. Ho Ko and K. Kim, *Chem. Commun.*, 2012, **48**, 11650–11652.

51 B. C. Ranu and U. Jana, *J. Org. Chem.*, 1998, **63**, 8212–8216.

52 T. Bunchuay, R. Ketkaew, P. Chotmongkolsap, T. Chutimasakul, J. Kanarat, Y. Tantirungrotechai and J. Tantirungrotechai, *Catal. Sci. Technol.*, 2017, **7**, 6069–6079.

53 J. Kim, R. G. Harrison, C. Kim and L. Que, *J. Am. Chem. Soc.*, 1996, **118**, 4373–4379.

54 U. Neuenschwander, F. Guignard and I. Hermans, *ChemSusChem*, 2010, **3**, 75–84.

55 X. Li, D. Ma, B. Cao and Y. Lu, *New J. Chem.*, 2017, **41**, 11619–11625.

56 W. Nam, H. J. Kim, S. H. Kim, R. Y. N. Ho and J. S. Valentine, *Inorg. Chem.*, 1996, **35**, 1045–1049.